Parameters estimation from the gravity anomaly caused by the two-dimensional horizontal thin sheet applying the global particle swarm algorithm

Khalid S Essa, Yves Géraud

Parameters estimation from the gravity anomaly caused by the two-dimensional horizontal thin sheet applying the global particle swarm algorithm

Khalid S. Essa [a,*], Yves Geraud [b]

[a] Department of Geophysics, Faculty of Science, Cairo University, Giza, P.O. 12613, Egypt [b] Université de Lorraine, CNRS, GeoRessources, F-54000 Nancy, France

ARTICLEINFO

Keywords:
Gravity anomaly
Depth
Width
Two-dimensional sheet
Oil exploration

ABSTRACT

A global particle swarm algorithm utilized to assess the inverted two-dimensional horizontal thin sheet parameters from the gravity anomaly profile based on applying the second moving average method. The using of the second moving average method has more advantageous than using the Bouguer gravity anomaly because this method has a capability in eliminating the regional field up to third-order impeded in the Bouguer anomaly. This algorithm is applied to interpret the gravity anomaly profile, i.e., estimating the depth, the width, the thickness, the density contrast and the origin location of the buried structure. The efficacy and stability of this method are investigated and exposed for utilizing free-noise and noisy synthetic examples. Real gravity data associated with oil and gas and mineral exploration from three different locations around the world is interpreted. The evaluated time to discovering this appropriate clarification is very short and the estimated parameters contrast the view that the proposed method is applicable for real exploration. It can extract the inverse parameters which have a geologic and economic significance.

1. Introduction

Gravity anomaly interpretation is beneficial in discover areas that have anomalous under the surface. Besides, the numerous application of gravity method in oil, gas, ores, and minerals exploration, engineering applications, geothermal ancient civilization investigations (Essa, 2013; Abdelfettah et al., 2014; Mehanee, 2014; Aydemir et al., 2015; Mehanee and Essa, 2015; Deng et al., 2016; Biswas et al., 2017; Al-Farhan et al., 2019). Gravity data interpretation is ill-posed and non-unique which is evident through various geometric-shapes of subsurface structures that can produce similar gravity anomaly at the surface of the earth. So, we minimize this non-uniqueness and ill-posedness by finding the desired geometry for subsurface targets with an identified density followed by the inversion process (Eshaghzadeh et al., 2019).

The target of this study is to discover and figure out the two- dimensional horizontal thin sheet, which resembles magma intrusion in sedimentary covers (Kearey et al., 2002). The evaluation of the depth, thickness, and width of the buried bodies is very important in assessing the importance of buried economic targets.

Many scientists showed and deliberated different methods for inferring gravity data due to this source (Skeels, 1963; Pick et al., 1973). Nevertheless, the shortcomings of these approaches that rely on specific points and curves are focus on human inaccuracies in figuring the parameters of the buried structures (Essa, 2014). So, there is still a necessity for an inversion elucidation method that is accurate, vigorous, fast and gives approximately real geometry parameters of the forms in field cases. In addition, the accuracy of appraising the depth and the width relies on the accuracy of separating the residual field from the observed gravity data.

Abdelrahman et al. (2016) established a least-squares algorithm to calculate simultaneously the depth and the width of a buried two-dimensional thin sheet from moving average residual gravity anomalies applying the window curves method. The main drawback of using the window curves method is entrapped in local minima. In other words, the intersection of the window curves intersect in different solution and sometimes not converge.

Thus, a gravity anomaly profile generated by a finite two- dimensional thin sheet was studied to infer the buried thin sheet parameters (the depth, width, thickness, the density, and the origin location) including a different level of noise (0%, 5%, 10%, 15%, and 20%)
and multi-sources to measure the robustness and the consistency of the suggested method. Besides, this method is confirmed by three field examples from Canada, Cameroon, and Iraq.

2. The method

The general observed gravity anomaly is represented by the following form:

$T_{otal}(x_j) = g(x_j; h; w) + R_{egional}(x_j); j = 0; 1; 2; 3; \ldots; N$ (1) where $T_{otal}(x_j)$ represented the collected gravity data, $g(x_j; h; w)$ represented the residual gravity anomaly for the two-dimensional thin sheet, which is mentioned below, and $R_{egional}(x_j)$ is the regional background field (Pawlowski, 1994; Obasi et al., 2016; Essa and Munschy, 2019).

2.1. The two-dimensional thin sheet model

The profile of gravity anomaly (mGal) generated by the finite two-dimensional horizontal thin sheet (Pick et al., 1973: Abdelrahman et al., 2016) along the profile is:

$$g(x_j, h, w) = 2G\Delta\sigma t\left\{tan^{-1}\left[\frac{w-2(x_j-c)}{2h}\right]+tan^{-1}\left[\frac{w+2(x_j-c)}{2h}\right]\right\}, \quad j=0, 1, 2, \ldots, N \tag{2}$$

where h is the depth to the center (m), w is the width of the sheet (m), x_j is the survey positions (m), c is location of the central point of the anomaly (m), $\Delta\sigma$ is the density contrast among the target and the surrounds $g_{=cc}$, G is the universal gravitational constant parameter that equals 6.67 $10^{11} m^3 kg\ s^2$, and t is the thickness (m). Fig. 1 shows a sketch for the two-dimensional

horizontal thin sheet and all parameters are demonstrated. *2.2. The second moving average method*

The second moving average method is considered as one of the pioneer methods in separating the regional background field, which is represented by a mathematical polynomial up to a third-order (Griffin, 1949; Essa and Munschy, 2019). The second moving average regional anomaly along the profile is:

$$R_2(x_j,z,s)=\frac{6g(x_j)-4g(x_j+s)-4g(x_j-s)+g(x_j+2s)+g(x_j-s)}{4}\ , \tag{3}$$

where s is the window lengths. Furthermore, the interpretation involves only a relatively long profile length, the problem of applying short profile lengths may be overcome effectively and economically by increasing the measurements number through the constrained length of the profile or digitizing the old gravity profile using a suitable interval.

2.3. The global optimization particle swarm algorithm

The global optimization particle swarm is developed and introduced during the last years to solve many geophysical problems (Sen and Stoffa, 2013; Singh and Biswas, 2016; Essa and Elhussein, 2018; Essa, 2019, 2020; Karcıoglu and Gürer, 2019). The particle swarm progression is stochastic and stirred by the communal repetitive in a journey of birds for searching the foods where the birds are the models. The individually model has a position and velocity vectors where the position vectors signify the value of the parameters. The particle swarm is adjusted with random models and looking for sources by apprising generations. In every iteration step, each model modernizes its velocity and place utilizing the next formulas:

$$V_j^{k+1}=c_3V_j^k+c_1\mathrm{rand}\left(T_{best}-P_j^{k+1}\right)+c_2\mathrm{rand}\left[\left(J_{best}-P_j^{k+1}\right)\right], \tag{4}$$

$$P_j^{k+1}=P_j^k+V_j^{k+1}\ . \tag{5}$$

where v^k_j is the j^{th} particle velocity at the k^{th} iteration, P^k_j is the present j^{th} particle place at the k^{th} iteration, rand is random numbers amongst ½0;1, c_1 *and* c_2 are cognitive and social parameters and equivalent 2 (Parsopoulos and Vrahatis, 2002), c_3 is the inertial coefficient that controls the particle velocity and its value ˂ 1. The inspiration behind selecting and utilizing the particle swarm technique is to get a global solution of various geometrical bodies from the gravity data quickly and point out the prominence of employing this technique between various conventional, non-conventional and optimization approaches. Furthermore, quick merging to the optimum solution in real time influence managing and well recital assessment. Then, synthetic and real examples mentioned-below have been examined to confirm the motivation of using the particle swarm method at any time in the future.

2.4. The two-dimensional thin sheet parameters calculation

The started model is gradually refined at every iterative-step to catch the optimum-fit amid the measured and the calculated data. For each step, the body parameters (h, w, t, Δσ, and c) are improved to catch the paramount values by minimizing the subsequent objective function. The optimal-solution of the body parameters (h, w, t, Δσ, and c) attained through applying the following objective function ðϕ_{obj}Þ

$$\phi_{obj}=\frac{1}{N}\sum_{i=1}^{N}\left[T_j^o(x_j)-T_j^p(x_j)\right]^2\ , \tag{6}$$

where N is the observed points, $T_j{}^o$ is the observed gravity anomaly and $T_j{}^p$ is the calculated gravity anomaly at the point x_j

Finally, after estimated the body parameters (h, w, t, Δσ, and c) of the buried two-dimensional thin sheet, the complete error (ψ) between the observed and calculated fields are assessed by taking the square-root of Eq. (6).

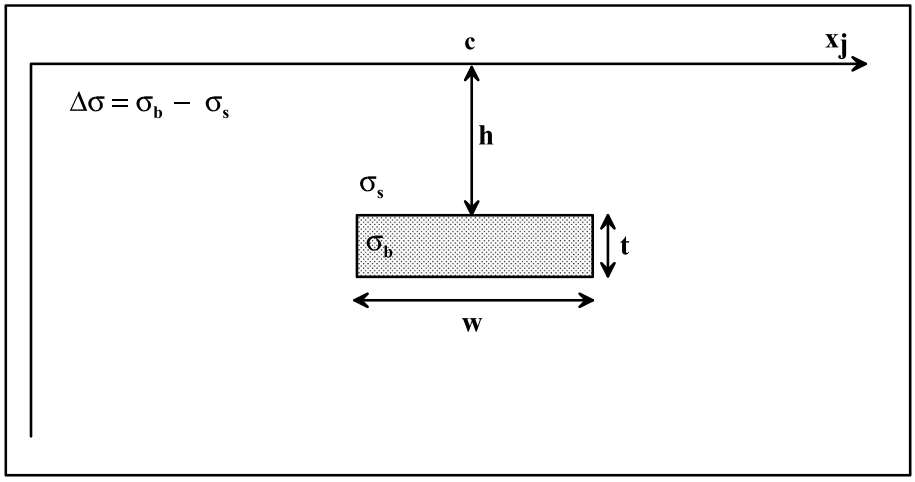

Fig. 1. A sketch diagram for the two-dimensional thin sheet including the model parameters.

3. Application to synthetic example

So, the examination of the accuracy and the benefits of the suggested approach were inspected through a synthetic finite two-dimensional thin sheet model of parameters: h ¼ 12 km, w ¼ 5 km, t ¼ 3 km, Δσ ¼ 1 $g_{=CC}$, c ¼ 5 km, and profile length ¼ 100 km generated and containing a third-order regional field applying the following equation:

$$\Delta g(x_j)=40.02\left\{tan^{-1}\left[\frac{5-2(x_j-5)}{24}\right]+tan^{-1}\left[\frac{5+2(x_j-5)}{24}\right]\right\} + \ 0.0003\,x_j^3+0.001x_j^2+0.01x_j+3\ . \tag{7}$$

Besides, this anomaly is subjected to various levels of noise 0%, 5%, 10%, 15%, and 20%. This gravity data inferred applying the global particle swarm algorithm using 100 models utilizing 100 particles. The optimum model parameters reached after 300 iterations and the range values of each parameter are demonstrated in Table 1. Table 1 validates the ranges of every parameter and the estimated results for each parameter at every window lengths (s-values). In addition, it shows the average value (ϕ_{avg}), uncertainty and percentage of error (E-value) in every parameter and the ψ-value that

reveals the misfit between the observed and computed anomalies. The achieved results for every parameter (h, w, t, Δσ, and c) are in an appropriate and close covenant amongst the actual and valued model parameters. This analysis is done to recover the actual two-dimensional thin sheet model parameters as follows:

Firstly, a noise-free (0%) gravity anomaly profile of a two- dimensional thin sheet model (Fig. 2a). This anomaly exposed to the second moving average method to exclude the effect of the regional field utilizing several window lengths (s ¼ 3, 4, 5, 6, 7, and 8 km) (Fig. 2b). After that, the particle swarm method is applied to achieve the thin sheet parameters (h, w, t, Δσ, and c) (Table 1). Table 1 shows the ranges of every parameter; the depth (h) is between 1 and 20 km, the width (w) is between 1 and 20 km, the thickness (t) is between 1 and 10 km, the density contrast (Δσ) is between 0.5 and 1.5 $g_{=cc}$, and the origin location of the buried body is between 1 and 20 km. Besides, Table 1 displays the estimated results for each parameter at every s-value, the average value (ϕ_{avg}), uncertainty, percentage error (E), and the root mean squared value (ψ), which reveals the misfit amongst the observed and the calculated anomalies. According to the results in Table 1 in this case, the E-values and ψ-value equal zero (Fig. 2k and l).

Secondly, in case of adding 5% random noise on the composite anomaly (Δg) (Fig. 2c), the second moving average method was used for the similar window lengths (s ¼ 3, 4, 5, 6, 7, and 8 km) to exclude the regional anomaly in this field (Fig. 2d). Moreover, it is interpreted by utilizing the particle swarm algorithm to assess the body parameters (Table 1). In Table 1, the ϕ_{avg}-values for h, w, t, Δσ, and c are 11.73 0.13 km, 4.86 0.06 km, 2.91 0.04 km, 0.96 0.02 $g_{=cc}$, and 4.79 0.07, the E-values are 2.21%, 2.90%, 3%, 4%, and 4.07% (Fig. 2k), respectively, and the ψ-value is 0.71 mGal. Besides, the misfit is figured in Fig. 2l.

Thirdly, we increased the level of noise to be 10% adding to the composite anomaly in equation (7) (Fig. 2e). Using the same procedures as above, the second moving averages residual anomalies are revealed in Fig. 2f and the results are tabulated and demonstrated in Table 1. From Table 1, the estimated ϕ_{avg}-values for h, w, t, Δσ, and c are 11.64 0.13 km, 4.79 0.05 km, 2.85 0.03 km, 0.94 0.02 $g_{=cc}$, and 4.71 0.04, the E-values are 3.03%, 4.17%, 5.11%, 6%, and 5.87% (Fig. 2k), respectively. The correlation between the observed and the calculated is estimated (the ψ-value is 2.90 mGal). Also, the difference (residual) between them is drawn in Fig. 2l.

Fourthly, a 15% random noise data was added to the composite anomaly (Fig. 2g). For the similar s-values (s ¼ 3, 4, 5, 6, 7, and 8 km), the second moving average residual gravity anomalies are presented in Fig. 2h. By utilizing the particle swarm algorithm for these noisy data, the outcomes of the source parameters (h, w, t, Δσ, and c) are presented (Table 1). The inferred outcomes in Table 1 represent the fitting among the observed and calculated, i.e., the ϕ_{avg}-values for h, w, t, Δσ, and c are 11.44 0.08 km, 4.61 0.08 km, 2.75 0.06 km, 0.89 0.03 $g_{=cc}$, and 4.56 0.04, the E-values are 4.67%, 7.83%, 8.44%, 10.33%, and 8.76% (Fig. 2k), respectively, and the ψ-value equals 2.80 mGal. The misfit amongst the observed and calculated anomalies are presented in Fig. 2l.

Lastly, more random noise data (20%) was added to the mention above composite anomaly (Fig. 2i). By applying the similar procedures declared above, the second moving average residual anomalies are presented in Fig. 2j and the results due to using the global particle swarm algorithm are also mentioned in Table 1. Table 1 shows that the estimated ϕ_{avg}-values for h, w, t, Δσ, and c are 11.17 0.09 km, 4.39 0.08 km, 2.55 0.06 km, 0.83 0.04 $g_{=cc}$, and 4.45 0.08, and the E- values are 6.89%, 12.07%, 14.89%, 17.33%, and 10.83% (Fig. 2k), respectively. The comparison between the observed gravity anomaly and the calculated are assessed (the ψ-value is 2.68 mGal). Also, the difference (residual) between them is drawn in Fig. 2l.

Finally, these achieved values for noise-free and noisy test cases for the two-dimensional thin sheet model express that the suggested combination methods between utilizing the second moving average method that eliminated the regional background and noise and the particle swarm optimization method, which estimate the model parameters are steady and robust.

4. The comparison between the suggested approach and the window curves method

We inspected the proficiency and robustness of the anticipated method by matching its solutions with those achieved by the window curves method (Abdelrahman et al., 2016). The main difference amongst the proposed method and the window curves method are summarized as the best-estimates of the model parameters (depth and width).

Fig. 3a shows a synthetic noisy (5% random noise impeded) for a two-dimensional thin sheet model of parameters: h ¼ 10 km, w ¼ 6 km, and profile length ¼ 50 km generated and containing a first-order regional background field applying the following equation:

$$\Delta g(x_j) = 200\left\{ tan^{-1}\left[\frac{6-2(x_j)}{20}\right] + tan^{-1}\left[\frac{6+2(x_j)}{20}\right]\right\} + \quad 2x_j + 10\,. \tag{8}$$

So, this composite gravity anomaly is subjected to the first moving average method that used in Abdelrahman et al. (2016) and the second moving average method that used in the suggested approach using several s-values (s ¼ 3, 4, 5, 6, 7, and 8 km) (Fig. 3b and c).

Firstly, we interpreted this gravity anomaly utilizing the window curves method (Abdelrahman et al., 2016) (Fig. 3d). Fig. 3d shows that two locations of intersect (two curves only) happens and no convergence at all. In other words, the results at the locations of intersection are summarized as follows: at location 1: h ¼ 9.3 km and w ¼ 6.4 km and at location 2: h ¼ 8.1 km and w ¼ 9.5 km.

For calculating the parameters (2GΔσtÞ, I developed the following form using the point x_j ¼ 0:

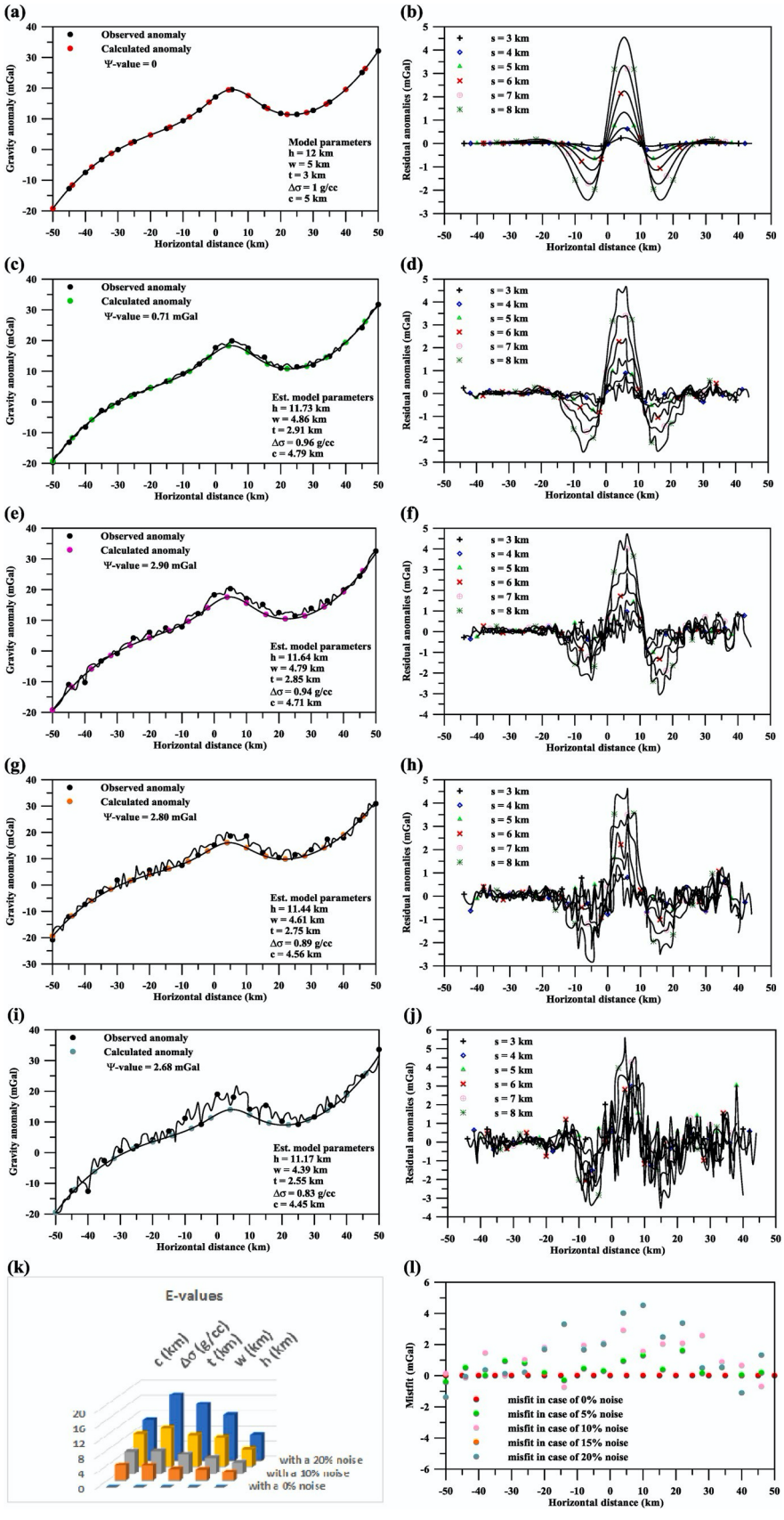

Fig. 2. (a) A composite synthetic gravity anomaly generated applying Eq. (7). (b) The second moving average residual gravity anomalies for a composite anomaly in Fig. 2a. (c) A noisy composite anomaly (5% noise added). (d) The second moving average residual gravity anomalies for a noisy composite anomaly in Fig. 2c. (e) A noisy composite anomaly (10% noise added). (f) The second moving average residual gravity anomalies for a noisy composite anomaly in Fig. 2e. (g) A noisy composite anomaly (15% noise added). (h) The second moving average residual gravity anomalies for a noisy composite anomaly in Fig. 2g. (i) A noisy composite anomaly (20% noise added). (j) The second moving average residual gravity anomalies for a noisy composite anomaly in Fig. 2i. (k) A diagram for the E-values in the model parameters in all cases mentioned above. (l) The misfit between the observed and calculated anomalies in all cases.

Table 1

Numerical results for applying the global particle swarm algorithm to interpret the second moving average residual gravity data using several s-values for a two- dimensional thin sheet model (h ¼ 12 km, w ¼ 5 km, t ¼ 3 km, Δσ ¼ 1 *g=cc*, c ¼ 5 km, and profile length ¼ 100 km) generated and containing a third-order regional background without and with various level of noise.

		Using the global particle swarm algorithm for interpreting gravity data								
parameters	Used ranges	with a 0% noise								
		s ¼ 3 km	s ¼ 4 km	s ¼ 5 km	s ¼ 6 km	s ¼ 7 km	s ¼ 8 km	ϕ^{avg}	E-value (%)	ψ (mGal)
			12.00	12.00	12.00	12.00	12.00			
h (km)	1-20	12.00						12.00 0	0	0
w (km)	1-20	5.00	5.00	5.00	5.00	5.00	5.00	5.00 0	0	
t (km)	1-10	3.00	3.00	3.00	3.00	3.00	3.00	3.00 0	0	
Δσ (g/cc)	0.5–1.5	1.00	1.00	1.00	1.00	1.00	1.00	1.00 0	0	
c (km)	1-10	5.00	5.00	5.00	5.00	5.00	5.00	5.00 0	0	
with a 5% noise										
h (km)	1-20	11.61	11.65	11.63	11.75	11.84	11.93	11.73 0.13	2.21	0.71
w (km)	1-20	4.76	4.81	4.87	4.83	4.91	4.95	4.86 0.06	2.90	
t (km)	1-10	2.85	2.89	2.88	2.93	2.95	2.96	2.91 0.04	3.00	
Δσ (g/cc)	0.5–1.5	0.95	0.96	0.95	0.95	0.97	0.98	0.96 0.01	4.00	
c (km)	1-10	4.70	4.78	4.74	4.79	4.85	4.92	4.79 0.07	4.07	
with a 10% noise										
h (km)	1-20	11.45	11.51	11.68	11.65	11.74	11.79	11.64 0.13	3.03	2.90
w (km)	1-20	4.72	4.74	4.83	4.78	4.84	4.84	4.79 0.05	4.17	
t (km)	1-10	2.81	2.83	2.83	2.83	2.87	2.91	2.85 0.03	5.11	
Δσ (g/cc)	0.5–1.5	0.92	0.92	0.95	0.94	0.95	0.96	0.94 0.02	6.00	

c (km)	1-10	4.62	4.66	4.71	4.68	4.76	4.81	4.71 0.07	5.87	
with a 15% noise										
h (km)	1-20	11.32	11.38	11.44	11.45	11.5	11.55	11.44 0.08	4.67	2.80
w (km)	1-20	4.53	4.55	4.55	4.61	4.69	4.72	4.61 0.08	7.83	
t (km)	1-10	2.66	2.69	2.75	2.77	2.78	2.83	2.75 0.06	8.44	
Δσ (g/cc)	0.5–1.5	0.86	0.88	0.88	0.9	0.93	0.93	0.89 0.03	10.33	
c (km)	1-10	4.53	4.51	4.56	4.56	4.6	4.61	4.56 0.04	8.76	
with a 20% noise										
h (km)	1-20	11.01	11.12	11.18	11.22	11.25	11.26	11.17 0.09	6.89	2.68
w (km)	1-20	4.3	4.33	4.38	4.41	4.42	4.54	4.39 0.08	12.07	
t (km)	1-10	2.51	2.51	2.5	2.57	2.58	2.65	2.55 0.06	14.89	
Δσ (g/cc)	0.5–1.5	0.78	0.79	0.81	0.83	0.87	0.88	0.83 0.04	17.33	
c (km)	1-10	4.36	4.38	4.44	4.49	4.53	4.55	4.45 0.08	10.83	

Table 2
Numerical results for applying the window curves method (Abdelrahman et al., 2016) to interpret the gravity anomaly generated using Eq. (8).

Parameters	Location 1	Location 2
2G Δσ t (mGal)	197.78	123.26
h (km)	9.3	8.1
w (km)	6.4	9.5
Ψ (mGal)	6.75	6.60

g

$$2G\Delta\sigma t = \frac{g\left(x_j, h, w\right)_{x_j=0}}{2\tan^{-1}\left(\frac{w_c}{h_c}\right)} \quad .$$

(9)

By using Eq. (9), the parameters (2*G*Δσ*t*Þ are equal 197.78 mGal and 123.26 mGal in locations 1 and 2, respectively (Table 2). The misfit between the observed and calculated anomalies due to the calculated results in two locations are presented in Fig. 3e. These are multi- solutions, which considered as the major disadvantage in applying the window curves method.

Secondly, applying the proposed method, the results of estimated model parameters (h, w, t, Δσ, and c) have been displayed in Table 3. Table 3 shows that the gauged ϕ_{avg}-values for h, w, t, Δσ, and c are 9.92 0.12 km, 6.02 0.09 km, 5.52 0.03 km, 2.71 0.02 *g=cc* and 0.02 0.01, and the ψ-value equals 2.16 mGal. The misfit between the observed and calculated anomalies is presented in Fig. 3f.

Finally, the results from applying our proposed method are more consistent than the result from utilizing the window curves method.

5. Application to multi-sources

The suggested method was tested on a composite gravity anomaly due to two thin sheets, which gives the same gravity anomaly to demonstrate its ability to distinguish between the two thin sheets (Fig. 4). Fig. 4a shows that the composite gravity anomaly consists of two thin sheets with the following parameters: the first body with h_1 ¼ 4.7 km, w_1 ¼ 2 km, t_1 ¼ 1.2 km, $\Delta\sigma_1$ ¼ 0.9 *g=cc*, c_1 ¼ 10 km, and profile length ¼ 70 km, the second body with h_2 ¼ 6 km, w_2 ¼ 4 km, t_2 ¼ 1 km, $\Delta\sigma_2$ ¼ 0.7 *g=cc*, c_2 ¼ 15 km, and profile length ¼ 70 km and generated applying the following form:

$$\Delta g(x_j) = 14.40\left\{ tan^{-1}\left[\frac{2-2(x_j-10)}{9.4}\right] + tan^{-1}\left[\frac{2+2(x_j-10)}{9.4}\right]\right\} + 9.34\left\{ tan^{-1}\left[\frac{4-2(x_j+15)}{12}\right] + tan^{-1}\left[\frac{4+2(x_j+15)}{12}\right]\right\}. \quad (10)$$

The interpretation procedures mentioned were applied to the composite gravity anomaly generated from Eq. (10) as follows: First in case of noise-free (Fig. 4a), the second moving average gravity anomalies were estimated using various window lengths (s ¼ 3, 4, 5, 6, 7, and 8 km) (Fig. 4b). Then, the two thin sheets sources parameters were calculated through the particle swarm method (Table 4). Table 4 displays the average results of each thin sheet source as h_1 ¼ 4.70 0.03 km, w_1 ¼ 2.03 0.06 km, t_1 ¼ 1.19 0.04 km, $\Delta\sigma_1$ ¼ 0.90 0.03 *g=cc*, c_1 ¼ 9.84 0.51 km for the body 1 and h_2 ¼ 6.18 0.09 km, w_2 ¼ 4.16 0.08 km, t_2 ¼ 1.04 0.02 km, $\Delta\sigma_2$ ¼ 0.72 0.01 *g=cc*, c_2 ¼ 15.24 0.18 km for the body 2. Also, the root mean squared value (ψ ¼ 0.24 mGal), which exposes the misfit between the observed and the calculated anomalies (Fig. 4f).

Secondly in case of adding a 10% random noise on the composite gravity anomaly profile (Fig. 4c). For the same window lengths values (s ¼ 3, 4, 5, 6, 7, and 8 km), the second moving average residual gravity anomalies are offered in Fig. 4d. After that, the particle swarm algorithm was applied to assess the thin sheets parameters (Table 4). The estimated

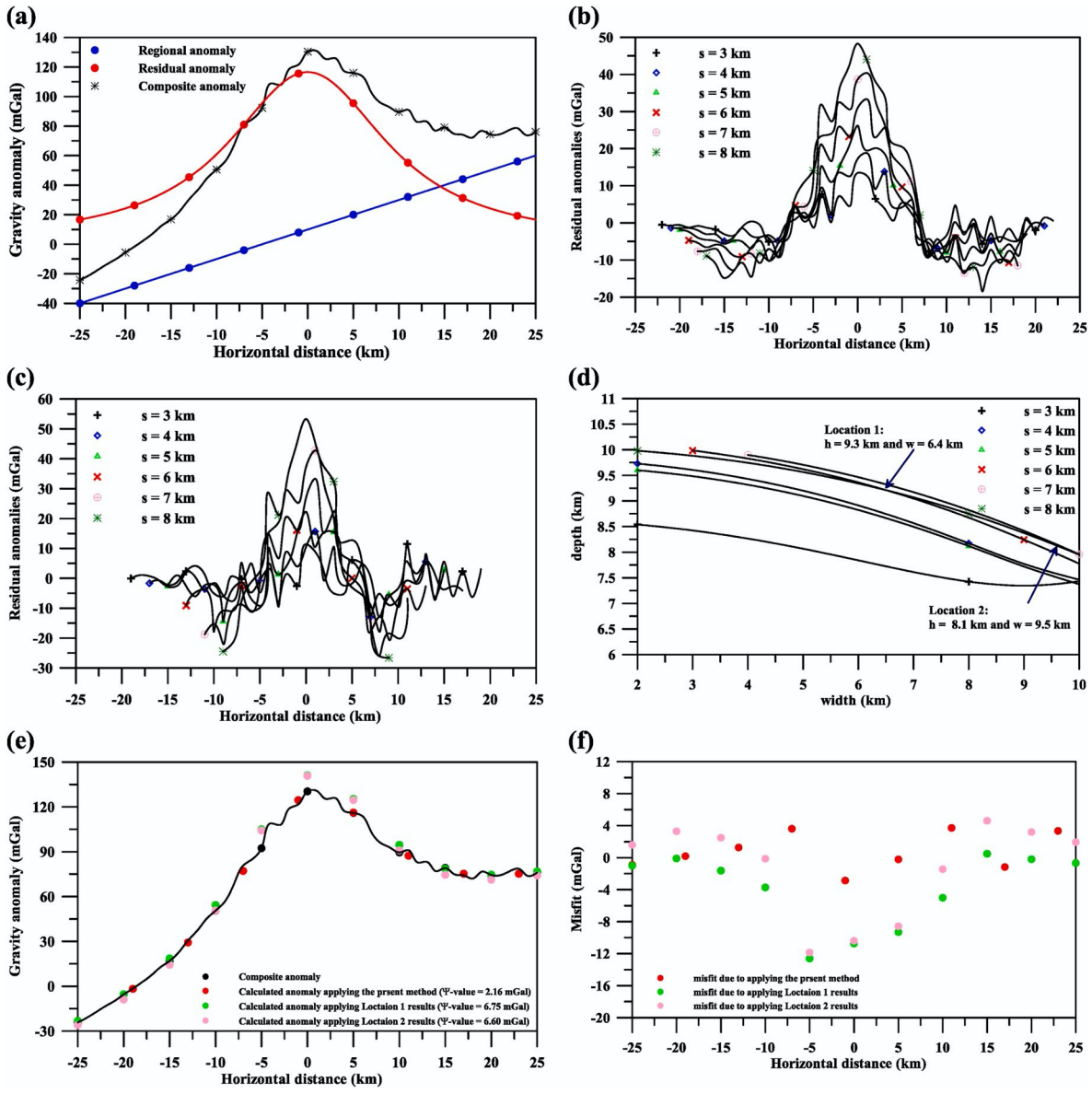

Fig. 3. (a) A composite noisy synthetic gravity anomaly generated applying Eq. (8). (b) The first moving average residual gravity anomalies for a composite anomaly in Fig. 3a. (c) The second moving average residual gravity anomalies for a composite anomaly in Fig. 3a. (d) The window curves results applying Abdelrahman et al. (2016) method. (e) The observed and calculated anomalies from applying the present method and Abdelrahman et al. (2016) method. (f) The misfit between the observed and calculated anomalies in all cases.

Table 3
Numerical results for applying the present approach to interpret the gravity anomaly generated using equation (8).

		Using the global particle swarm algorithm for interpreting gravity data							
parameters	Used ranges	s ¼ 3 km with a 0% noise	s ¼ 4 km	s ¼ 5 km	s ¼ 6 km	s ¼ 7 km	s ¼ 8 km	ϕ_{avg}	Ψ (mGal)
h (km)	1-20	9.72	9.84	10.02	10	9.96	9.98	9.92 0.12	2.16
w (km)	1-20	5.86	5.94	6.11	6.05	6.06	6.08	6.02 0.09	
t (km)	1-10	5.46	5.49	5.5	5.53	5.52	5.52	5.50 0.03	
Δσ (g/cc)	0.5–1.5	2.68	2.69	2.71	2.73	2.72	2.73	2.71 0.02	
c (km)	1-10	0.05	0.03	0.02	0.01	0.01	0.02	0.02 0.01	

parameters signify the optimal fitting between the observed and calculated anomalies. In other words, the ϕ_{avg}-values for each parameter are h_1 ¼ 4.60 0.413 km, w_1 ¼ 2.07 0.13 km, t_1 ¼ 1.22 0.09 km, $\Delta\sigma_1$ ¼ 0.87 0.08 $g_{=cc}$, c_1 ¼ 9.76 0.82 km for the body 1 and h_2 ¼ 6.29 0.51 km, w_2 ¼ 4.23 0.38 km, t_2 ¼ 1.05 0.17 km, $\Delta\sigma_2$ ¼ 0.73 0.06 $g_{=cc}$, c_2 ¼ 15.43 0.64 km for the body 2 (Fig. 4c). Also, the ψ-value equals 0.62 mGal. The misfit amongst the observed and calculated anomalies is presented in Fig. 4f.

Finally, the applicability of this method to the multi-solution problem of gravity inversion reveals that the proposed method has the capability and possibility to distinguish the multi-thin sheets sources.

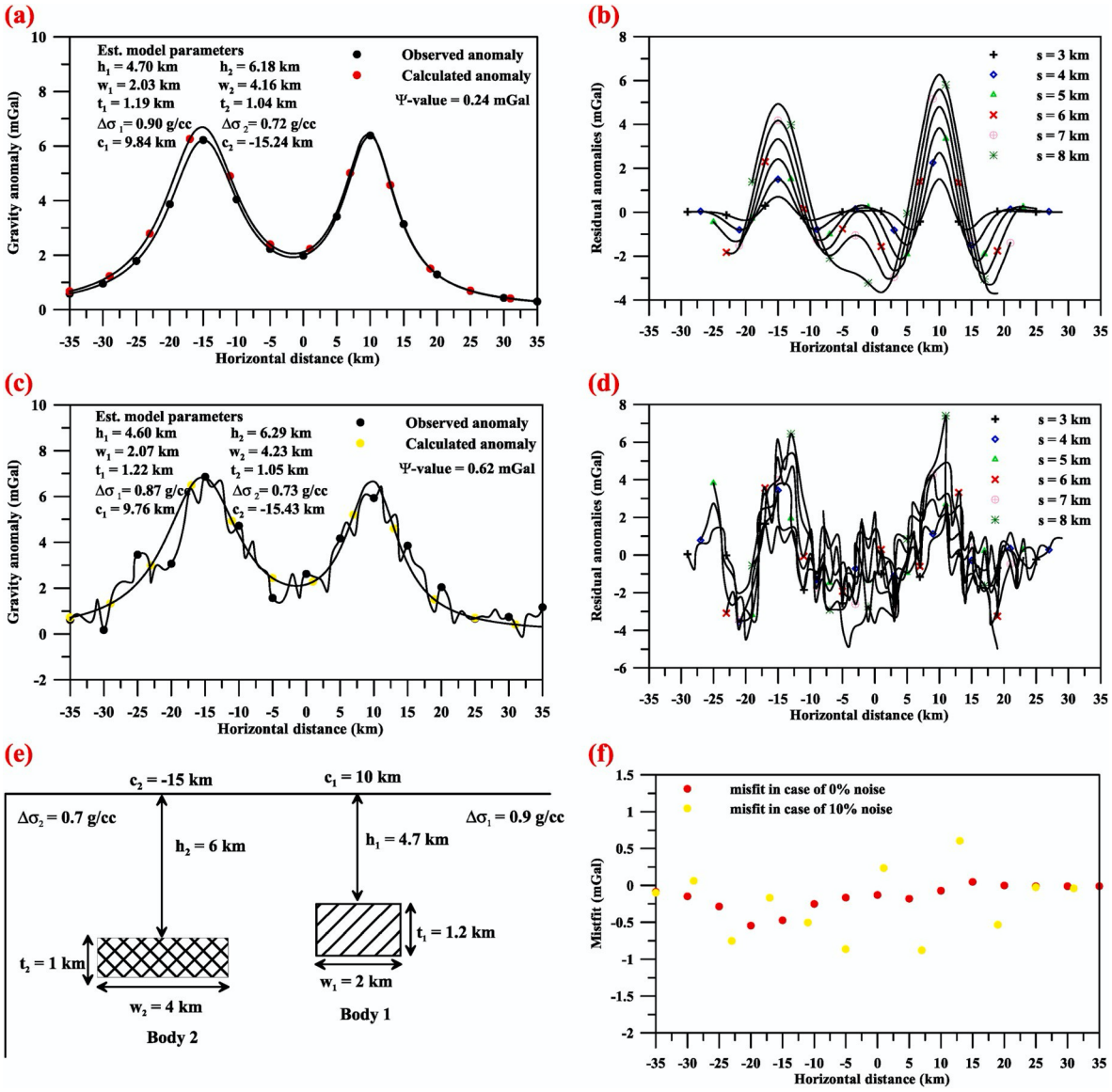

Fig. 4. (a) A composite synthetic gravity anomaly generated applying Eq. (10) for multi-thin sheets. (b) The second moving average residual gravity anomalies for a composite anomaly in Fig. 4a. (c) A noisy composite anomaly (10% noise added). (d) The second moving average residual gravity anomalies for a noisy composite anomaly in Fig. 4c. (e) A sketch diagram for the buried two thin sheets. (f) The misfit between the observed and calculated anomalies in all cases.

6. Application to field examples

The new method is prepared and adjusted for examining observed gravity anomalies due to a two-dimensional horizontal thin sheet. Three field examples from Canada, Cameroon, and Iraq have been re- elucidated to study the robustance and constancy of the method.

6.1. Oil and gas field example, Canada

The area of this study is situated in the northeast Canadian Appalachians that is affected by numerous orogenic events with a complicated geological history, punctuated by the opening and closing of the Iapetus Ocean. Williams (1979) divided the Canadian Appalachians into five tectono-stratigraphic domains including the Newfoundland area.

A Bouguer gravity anomaly profile over oil and gas field example, Portland Creek Pond, Northern Newfoundland, Canada (Telford et al., 1990) (Fig. 5a). This profile is 2621.3 m in length. The gravity curve was digitized at an equal interval of 61 m. The suggested algorithm was exploited to the gravity data to assess the buried model parameters (h, w, t, Δσ, c) via the second residual gravity anomalies of the gravity data. The results are demonstrated and shown in Table 5. This anomaly exposed to the second moving average method to remove the effect of regional field utilizing several window lengths (s ¼ 243.8, 304.8, 365.8, 426.8, 487.8, 548.8, and 609.8 m) (Fig. 5b). After that, the global particle swarm optimization method is applied to achieve the buried body parameters (Table 5). Table 5 shows the ranges of every parameter and the estimated results for each parameter at every s-value, the average value (ϕ_{avg}), uncertainty, and the ψ-value, which demonstrates the misfit amongst the observed and the calculated anomalies. The forward model due to the estimated parameters is drawn in Fig. 5a and a sketch diagram showing the buried finite two-dimensional thin sheet (Fig. 5c) to show the misfit between them (Fig. 5d). According to the misfit between the observed and the calculated anomalies (Fig. 5a), which shows large discrepancies in the right half of curves. This discrepancy may be due to the effect of very nearer other structures. But still, the suggested method gives a good view of the subsurface geologic structures.

Table 4
Numerical results for applying the global particle swarm algorithm to interpret the second moving average residual gravity data using several s-values for the multi- thin sheet models without and with a 10% noise.

Using the global particle swarm algorithm for interpreting gravity data											
Model	parameters	Used ranges	with a 0% noise								
			s ¼ 3 km	s ¼ 4 km	s ¼ 5 km	s ¼ 6 km	s ¼ 7 km	s ¼ 8 km	ϕ_{avg}	E-value (%)	Ψ (mGal)
Body 1	h_1 (km)	1–20	4.65	4.71	4.7	4.73	4.72	4.71	4.70 0.03	0.07	0.24
	w_1 (km)	1–20	1.94	1.99	2.05	2.11	2.06	2.03	2.03 0.06	1.50	
	t_1 (km)	1–10	1.12	1.18	1.22	1.24	1.2	1.18	1.19 0.04	0.83	
	$\Delta\sigma_1$ (g/cc)	0.1–1.5	0.85	0.9	0.9	0.91	0.93	0.92	0.90 0.03	0.19	
	c_1 (km)	35-þ35	8.92	9.57	10.12	10.23	10.09	10.1	9.84 0.51	1.62	
Body 2	h_2 (km)	1–20	6.13	6.22	6.06	6.17	6.34	6.17	6.18 0.09	3.03	
	w_2 (km)	1–20	4.03	4.15	4.18	4.09	4.26	4.23	4.16 0.08	3.91	
	t_2 (km)	1–10	1.02	1.05	1.03	1.06	1.04	1.01	1.04 0.02	3.50	
	$\Delta\sigma_2$ (g/cc)	0.1–1.5	0.72	0.73	0.71	0.71	0.73	0.72	0.72 0.01	2.86	
	c_2 (km)	35-þ35	15.1	15.32	15.53	15.27	15.19	15.03	15.24 0.18	1.60	
with a 10% noise											
Body 1	h_1 (km)	1–20	3.98	4.25	4.72	4.86	5.06	4.75	4.60 0.41	2.06	0.62
	w_1 (km)	1–20	1.86	2.03	2.12	2.25	2.13	2.04	2.07 0.13	3.58	
	t_1 (km)	1–10	1.07	1.18	1.23	1.29	1.32	1.22	1.22 0.09	1.53	
	$\Delta\sigma_1$ (g/cc)	0.1–1.5	0.72	0.86	0.91	0.93	0.93	0.85	0.87 0.08	3.70	
	c_1 (km)	35-þ35	8.54	9.1	9.68	10.13	10.67	10.43	9.76 0.82	2.42	
Body 2	h_2 (km)	1–20	5.43	5.99	6.45	6.88	6.61	6.4	6.29 0.51	4.89	
	w_2 (km)	1–20	3.71	4.01	4.36	4.81	4.41	4.11	4.23 0.38	5.87	
	t_2 (km)	1–10	0.79	0.91	1.07	1.18	1.26	1.1	1.05 0.17	5.17	
	$\Delta\sigma_2$ (g/cc)	0.1–1.5	0.63	0.7	0.76	0.81	0.74	0.75	0.73 0.06	4.52	
	c_2 (km)	35-þ35	14.42	15.12	15.91	16.27	15.54	15.31	15.43 0.64	2.86	

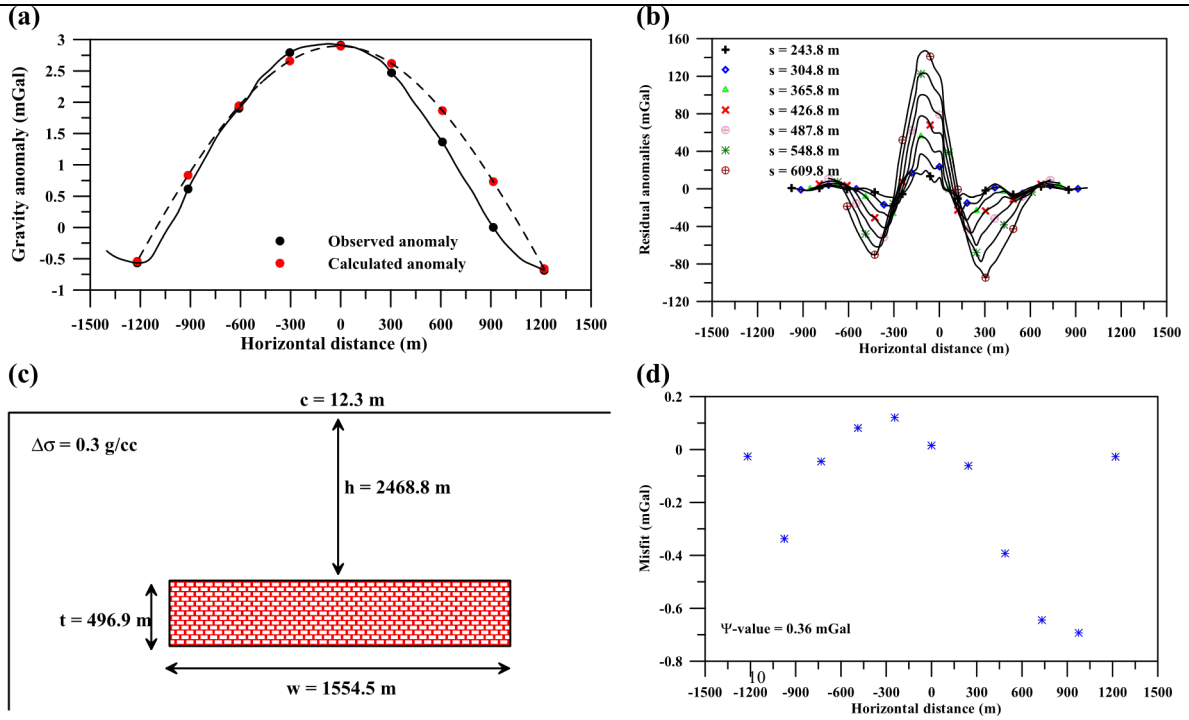

Fig. 5. (a) A gravity anomaly profile collected over oil and gas field example, Portland Creek Pond, Northern Newfoundland, Canada (after Telford et al., 1990). (b) The second moving average residual gravity anomalies of the anomaly in Fig. 5a. (c) A sketch diagram for the buried model resulted from the suggested approach. (d)

The misfit between the observed and calculated anomalies.

6.2. Basaltic intrusion body, Cameroon

Fig. 6a shows a gravity anomaly profile (A-A) collected in the Logone Birni Basin in the West and Central African rift system, Northernmost Cameroon (Albert et al., 2019). This basin is characterized by polyphase rifting isolated by structural tectonic events that can be recognized as regional folding deformation, hiatus of sedimentation and non-conformities in both seismic interpretation and outcrops. Moreover, this basin is the product of a complicated time for the distribution of the continents, as Africa responded to the plate tectonic fragmentation of the Gondwana. Also, a distribution of covered volcanic bodies just as their associations with the structural and tectonic evolution of this basin. The volcanic activity during this basin is confined to the Cretaceous age (Mkoumbe et al., 2019). Loule and Pospisil (2013) have described the magmatic activity in the area of study has been related to the evolution of the Logone Birni Basin that occurred in the Cretaceous time. Ngounouno et al. (2000) testified that most of the resulted igneous rocks were small in size. If the causative body is an igneous intrusive, similar to those inferred from the tectonic history of the Logone Birni Basin (Benkhelil, 1982; Avbovbo et al., 1986; Genik, 1992), then the lateral extension of the causative body could be smaller than that observed in our model, even though igneous intrusions may be highly variable in shape and composition. It is unlikely, however, even if the anomaly is caused by an intrusion, that it is related to the evolution of the Logone Birni Basin.

The gravity profile length is 40,000 m and digitized at an interval of 1000 m for the present interpretation. The interpretation procedure revealed above is again applied for this data. For several s-value (s ¼ 2000, 3000, 4000, 5000, and 6000 m), the second moving average residual gravity anomalies were created (Fig. 6b). The global particle swarm algorithm was utilized for these anomalies to assess the target parameters (Table 6). The geologic cross-section for the estimated model is presented in Fig. 6c and the misfit between the observed and calculated anomalies is presented in Fig. 6d. The expected parameters of the body by applying the suggested method convolved with the moving average method have a good agreement with the results accomplished by Albert et al. (2019) method.

Table 6

Numerical results for applying the present approach to interpret to the gravity anomaly for the Logone Birni Basin in Northernmost Cameroon.

parameters	Used ranges	Using the global particle swarm algorithm for interpreting gravity data							
		s ¼ 243.8 m	s ¼ 304.8 m	s ¼ 365.8 m	s ¼ 426.8 m	s ¼ 487.8 m	s ¼ 548.8 m	s ¼ 609.8 m	ϕ_{avg} Ψ (mGal)
h (m)	609.6–3657.6	2453.8	2462.5	2467.7	2472.6	2479.9	2475.6	2469.3	2468.8 8.7 0.36 w (m) 304.8–3048 1515.0
	1522.8 1543.6	1554.7	1573.8	1583.4	1588.2	1554.5 28.9			
t (m)	304.8–3048	472.74	487.5	496.9	496.4	502.3	510.2	512.1	496.9 ± 13.6
Δσ (g/cc)	0.1–1.5	0.25	0.25	0.28	0.32	0.32	0.33	0.34	0.30 ± 0.04
c (m)	6.1–61	10.7	11.9	12.4	12.6	13.3	12.8	12.6	12.3 ± 0.8

Table 5

Numerical results for applying the present approach to interpret to the gravity anomaly for over oil and gas field example, Portland Creek Pond, Northern Newfoundland, Canada.

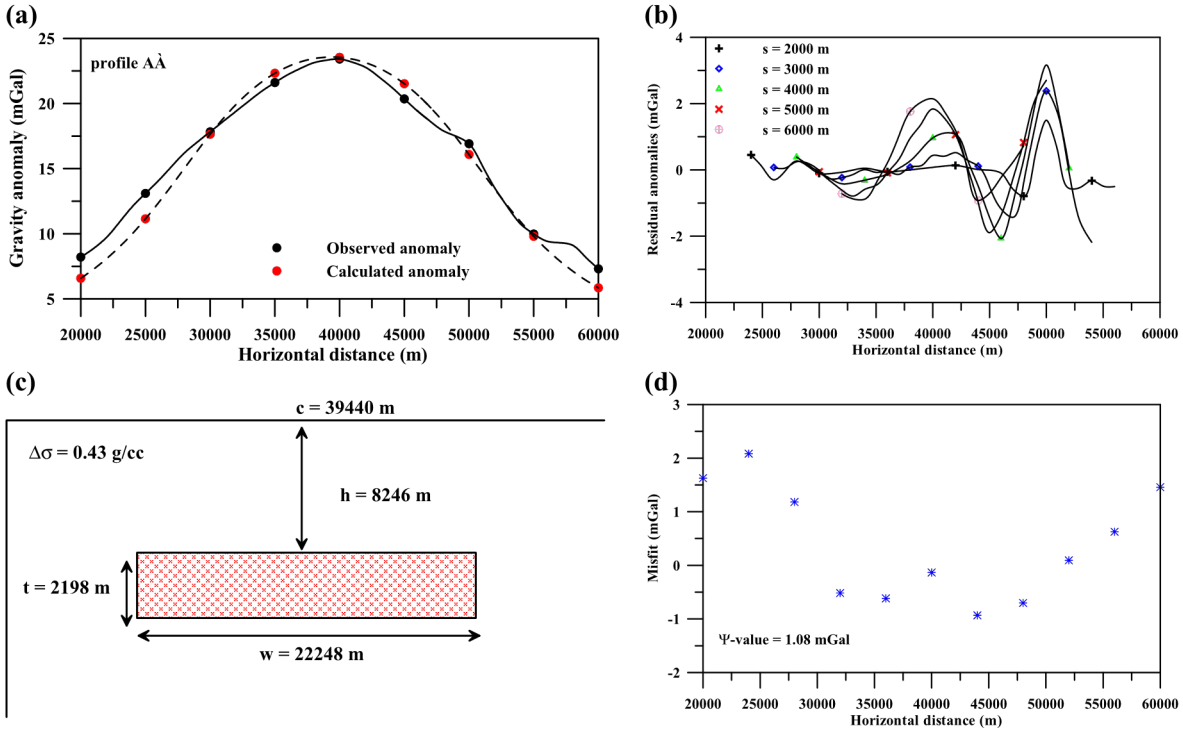

Fig. 6. (a) A gravity anomaly profile collected in the Logone Birni Basin in Northernmost Cameroon, Cameroon (after Albert et al., 2019). (b) The second moving average residual gravity anomalies of the anomaly in Fig. 6a. (c) A sketch diagram for the buried model resulted from the suggested approach. (d) The misfit between the observed and calculated anomalies.

6.3. Kifl oil field example, Iraq

The Kifl area is situated in the central of Iraq. It is characterized a sequence of sediments ranging from 7000 to 8000 m overlying the

parameters	Used ranges	Using the global particle swarm algorithm for interpreting gravity data						
		s ¼ 2000 m	s ¼ 3000 m	s ¼ 4000 m	s ¼ 5000 m	s ¼ 6000 m	ϕ_{avg}	Ψ (mGal)
h (m)	5000–30,000	8130	8210	8250	8290	8350	8246 82.9	1.08
w (m)	10,000-50,0000	22,030	22,130	22,260	22,350	22,470	22,248 174.1	
t (m)	1000–20,000	2110	2130	2190	2240	2320	2198 85.3	
Δσ (g/cc)	0.1–2.0	0.41	0.42	0.41	0.43	0.46	0.43 0.02	
c (m)	20,000-60,0000	38,800	39,200	39,500	39,600	40,100	39,440 482.7	

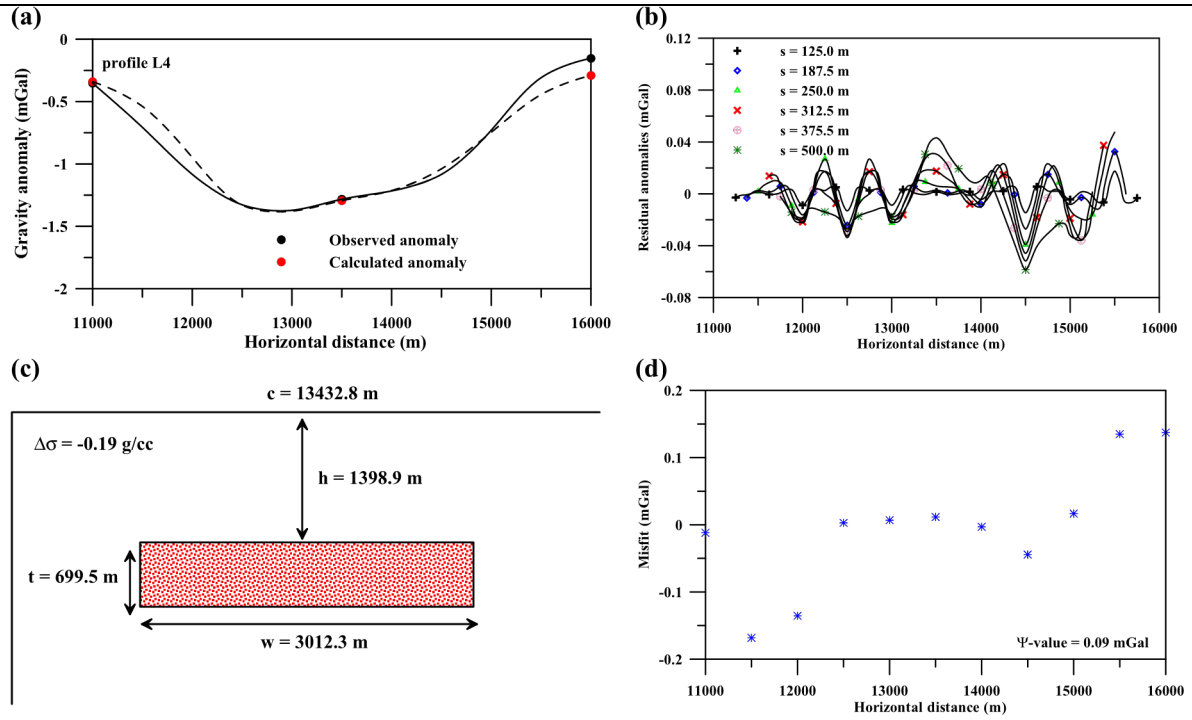

Fig. 7. (a) A gravity anomaly profile collected in the Kifl Oil field, Iraq (after Al-Farhan et al., 2019). (b) The second moving average residual gravity anomalies of the anomaly in Fig. 7a. (c) A sketch diagram for the buried model resulted from the suggested approach. (d) The misfit between the observed and calculated anomalies.

basement rocks. These sediments distributed as from Eocene in the southwest and recent deposits in the east (the Euphrates zone). Moreover, the Quaternary sediments covered most of the area and the below- formations are faulted. These fault are belonging to the Euphrates zone and its related to the prominent Najd fault (Sissakian and Mohammed, 2007; Fouad, 2010). The Kifl area is laying in the unstable shelf within Mesopotamia zone and Tigris subzone and considered as the boundary between stable and unstable shelf. This Mesopotamia intercontinental basin was developed inside the Arabian plate and to the west of the Zagros thrust zone. Therefore, the Kifl area was exaggerated by those movements and located on the west flank of the Mesopotamia basin (Buday and Jassim, 1987; Jassim and Goff, 2006; Mousa et al., 2017).

The gravity profile of line 4 (Al-Farhan et al., 2019, Fig. 12d) was taken for the present interpretation. This profile has a length of 5000 m and was digitized at 62.5 m sampling intervals (Fig. 7a). The mentioned-above interpretation procedures were applied as follows: first, the second moving average residual gravity anomalies were calculated applying various s-values (s ¼ 125, 187.5, 250, 312.5, 375, 437.5, and 500 m) (Fig. 7b). Second, the global particle swarm algorithm was used for these anomalies to estimate the target parameters (Table 7). The geological model is presented in Fig. 7c, which was produced from the estimated parameters and the misfit amongst the observed and calculated anomalies is demonstrated in Fig. 7d. Finally, the estimated model parameters of the buried target by applying the suggested method convolved with the moving average method have a good agreement with the results from Al-Farhan et al. (2019) method.

Finally, the suggested method has been applied successful in interpreting the real data due to a two-dimensional thin sheet for oil, gas, and mineral exploration in Canada, Cameroon, and Iraq that indicate that this method can be extended to investigate more regions around the world.

7. Conclusion

Table 7

Numerical results for applying the present approach to interpret to the gravity anomaly for the Kifl oil field example, Iraq.

parameters	Used ranges	Using the global particle swarm algorithm for interpreting gravity data								
		s ¼ 125 m	s ¼ 187.5 m	s ¼ 250 m	s ¼ 312.5 m	s ¼ 375 m	s ¼ 437.5 m	s ¼ 500 m	ϕ_{avg}	Ψ (mGal)
h (m)	500–5000	1368.7	1389.1	1401.3	1423.2	1411.9	1400	1397.8	1398.9 17.2	0.09
w (m)	500–10,000	2871.4	2914.9	2986.7	3037.9	3090.3	3128.1	3056.5	3012.3 93.2	
t (m)	100–2000	649.7	674.4	691.9	707.5	716.1	725.2	731.6	699.5 29.4	
Δσ (g/cc)	0.1–1.0	0.18	0.19	0.2	0.21	0.19	0.2	0.2	0.19 0.01	
c (m)	11,000-16,0000	13411.9	13415.6	13425.3	13433.4	13442.8	13451.76	13448.9	13432.8 15.9	

The suggested global optimization is performed to assess the depth, the width, the thickness, the density, and the location of buried two- dimensional thin sheet structures from the gravity anomaly. This method in the first relies on estimating the second moving average gravity residual anomalies utilizing the several window lengths. Secondly, applying the global particle swarm algorithm to estimate the target parameters. This method is less sensitive to noise and eliminating the regional background effect. Synthetic data (including noise), multi- sources and three field data (oil and gas example and mineralized example) are offered in our study to show and reveal the stability and efficiency of this method. Thus, the estimated inverse parameters should be engaged by geological information and others offered geophysical results to support in resolving any encountered unusual solution in geophysical exploration. Although this suggested method was applied for the oversimplified model, it gives a pertinent description for the geologic subsurface. Finally, because of the above facts, we will extend the application of this method in solving various problems in the future related to potential field data interpretation.

Declaration of competing interest

The authors declare that they have no known competing financial interests or personal relationships that could have appeared to influence the work reported in this paper.

CRediT authorship contribution statement

Khalid S. Essa: Conceptualization, Methodology, Writing - original draft, Writing - review & editing. **Yves Geraud:** Writing - review & editing, Visualization.

Acknowledgments

Authors would like to thank Prof. Prof. Vural Sander Suicmez, Editor- in-Chief, Prof. Rouhi Farajzadeh, Executive Editor, and, and the two anonymous expert reviewers for their keen interest and valuable comments for improving the original manuscript. Also, I wish to thank the Science and Technology Development Fund (STDF) and the Institut Francais d'Egypte (IFE) for providing a full support to finish this work. **Appendix A. Supplementary data**

Supplementary data to this article can be found online at https://doi.org/10.1016/j.petrol.2020.107421.

References

Abdelfettah, Y., Schill, E., Kuhn, P., 2014. Characterization of geothermally relevant structures at the top of crystalline basement in Switzerland by filters and gravity forward modelling. Geophys. J. Int. 199, 226–241.

Abdelrahman, E.M., Gobashy, M.M., Essa, K.S., Abo-Ezz, E.R., El-Araby, T.M., 2016. A least-squares minimization approach to interpret gravity data due to 2D horizontal thin sheet of finite width. Arab. J. Geosci. 9, 515.

Albert, E., Antoine, B.C., Eugene, L.D.A., Jacques, N.J., Alain, Z., Tabod, T.C., 2019. Understanding the meaning of the positive bouguer anomaly of waza (Northernmost Cameroon, central Africa). J. Geosci. Environ. Protect. 7, 55–65.

Al-Farhan, M., Oskooi, B., Ardestani, V.E., Abedi, M., Al-Khalidy, A., 2019. Magnetic and gravity signatures of the Kifl oil field in Iraq. J. Petrol. Sci. Eng. 183, 106397.

Avbovbo, A.A., Ayoola, E.O., Osahon, G.A., 1986. Depositional and structural styles in Chad basin of northeastern Nigeria. AAPG Bull. 70, 1787–1798.

Aydemir, A., Tigli, C.S., Ates, A., 2015. Integrated geophysical investigation of the Galatian basin around Seben region, Bolu, Turkey. J. Petrol. Sci. Eng. 129, 243–253.

Benkhelil, J., 1982. Benue trough and benue chain. Geol. Mag. 119, 158–168.

Biswas, A., Parija, M.P., Kumar, S., 2017. Global nonlinear optimization for the interpretation of source parameters from total gradient of gravity and magnetic anomalies caused by thin dyke. Ann. Geophys. 60, G0218.

Buday, T., Jassim, S.Z., 1987. The Regional Geology of Iraq: Tectonism, Magnetism, Metamorphism, and Min. Invest., p. 352. Geosurv. Baghdad, Iraq. in English.

Deng, Y., Chen, Y., Wang, P., Essa, K.S., Xub, T., Liang, X., Badal, J., 2016. Magmatic underplating beneath the Emeishan large igneous province (South China) revealed by the COMGRA-ELIP experiment. Tectonophysics 672–673, 16–23.

Eshaghzadeh, A., Dehghanpour, A., Sahebari, S.S., 2019. Marquardt inverse modeling of the residual gravity anomalies due to simple geometric structures: a case study of chromite deposit. Contrib. Geophys. Geodes. 49, 153–180.

Essa, K.S., 2013. Gravity interpretation of dipping faults using the variance analysis method. J. Geophys. Eng. 10, 015003.

Essa, K.S., 2014. New fast least-squares algorithm for estimating the best-fitting parameters due to simple geometric-structures from gravity anomalies. J. Adv. Res. 5, 57–65.

Essa, K.S., 2019. A particle swarm optimization method for interpreting self potential anomalies. J. Geophys. Eng. 16, 463–477.

Essa, K.S., 2020. Self potential data interpretation utilizing the particle swarm method for the finite 2D inclined dike: mineralized zones delineation. Acta Geod. Geophys. https://doi.org/10.1007/s40328-020-00289-2.

Essa, K.S., Elhussein, M., 2018. PSO (particle swarm optimization) for interpretation of magnetic anomalies caused by simple geometrical structures. Pure Appl. Geophys. 175, 3539–3553.

Essa, K.S., Munschy, M., 2019. Gravity data interpretation using the particle swarm optimization method with application to mineral exploration. J. Earth Syst. Sci. 128, 123.

Fouad, S.F.A., 2010. Tectonic and Structural Evolution of the Mesopotamia Foredeep (Iraq).

Genik, G.J., 1992. Regional framework, structural and petroleum aspects of rift basins in Niger, Chad and Central African Republic (C.A.R.). Tectonophysics 213, 169–185.

Griffin, W.R., 1949. Residual gravity in theory and practice. Geophysics 14, 39–58.

Jassim, S.Z., Goff, J.C., 2006. Geology of Iraq. Czech Republic. 80-7028-287-8pp. 341.

Karcıoglu, G., Gürer, A., 2019. Implementation and model uniqueness of Particle Swarm Optimization method with a 2D smooth modeling approach for Radio- Magnetotelluric data. J. Appl. Geophys. 169, 37–48.

Kearey, P., Brooks, M., Hill, I., 2002. An Introduction to Geophysical Exploration. Blackwell Science, p. 262.

Loule, J.P., Pospisil, L., 2013. Geophysical evidence of cretaceous volcanics in Logone Birni Basin (northern Cameroon), central Africa, and consequences for the west and central African rift system. Tectonophysics 583, 88–100.

Mehanee, S.A., 2014. Accurate and efficient regularized inversion approach for the isolated gravity anomalies. Pure Appl. Geophys. 171, 1897–1937.

Mehanee, S.A., Essa, K.S., 2015. 2.5D regularized inversion for the interpretation of residual gravity data by a dipping thin sheet: numerical examples and case studies with an insight on sensitivity and non-uniqueness. Earth Planets Space 67, 130.

Mkoumbe, E., Fosso Teguia, M.E.E., Eyike Yomba, A., Njandjock Nouck, P., Tabod, T.C., 2019. Depositional and structural styles in the Logone Birni Basin (LBB), northern Cameroon, from 3D potential field modeling: preliminary results. Open J. Geol. 9, 226–244.

Mousa, A., Mickus, K., Al-Rahim, A., 2017. The thickness of cover sequences in the Western Desert of Iraq from a power spectrum analysis of gravity and magnetic data. J. Asian Earth Sci. 138, 230–245.

Ngounouno, I., Deruelle, B., Demaiffe, D., 2000. Petrology of the bimodal cainozoic volcanism of the kapsiki plateau (Northernmost Cameroon, central Africa). J. Volcanol. Geoth. Res. 102, 21–44.

Obasi, A.I., Onwuemesi, A.G., Romanus, O.M., 2016. An enhanced trend surface analysis equation for regional–residual separation of gravity data. J. Appl. Geophys. 135, 90–99.

Parsopoulos, K.E., Vrahatis, M.N., 2002. Recent approaches to global optimization problems through particle swarm optimization. Nat. Comput. 1, 235–306.

Pawlowski, R.S., 1994. Green's equivalent-layer concept in gravity bandpass filter design. Geophysics 59, 69–76.

Pick, M., Picha, J., Vyskocil, V., 1973. Theory of the Earth's Gravity Field. Academia Publishing House of the Czechoslovak Academy of Sciences, Prague, p. 538.

Sen, M.K., Stoffa, P.L., 2013. Global Optimization Methods in Geophysical Inversion. Cambridge University Press, Cambridge, p. 289.

Singh, A., Biswas, A., 2016. Application of global particle swarm optimization for inversion of residual gravity anomalies over geological bodies with idealized geometries. Nat. Resour. Res. 25, 297–314.

Sissakian, V.K., Mohammed, B.S., 2007. Geology of Iraqi western desert. Iraqi Bull. Geol. Min. Spec. Issue 51–124.

Skeels, D.C., 1963. An approximation solution of the problem of maximum depth in gravity interpretation. Geophysics 28, 724–735.

Telford, W.M., Geldart, L.P., Sheriff, R.E., 1990. Applied Geophysics, second ed. Cambridge University Press, p. 770.

Williams, H., 1979. Appalachian Orogen in Canada. Can. J. Earth Sci. 16, 792–807.